entropy

MDPI

Article

Dynamic Mechanical Properties and Microstructure of an $(Al_{0.5}CoCrFeNi)_{0.95}Mo_{0.025}C_{0.025}$ High Entropy Alloy

Bingfeng Wang [1,2], Chu Wang [2], Bin Liu [1] and Xiaoyong Zhang [1,*]

[1] State Key Laboratory for Powder Metallurgy, Central South University, Changsha 410083, China; wangbingfeng@csu.edu.cn (B.W.); binliu@csu.edu.cn (B.L.)

[2] School of Materials Science and Engineering, Central South University, Changsha 410083, China; wangchu@csu.edu.cn

* Correspondence: zhangxiaoyong@csu.edu.cn; Tel.: +86-731-88876244

Received: 3 November 2019; Accepted: 25 November 2019; Published: 26 November 2019

Abstract: The dynamic mechanical properties and microstructure of the $(Al_{0.5}CoCrFeNi)_{0.95}Mo_{0.025}C_{0.025}$ high entropy alloy (HEA) prepared by powder extrusion were investigated by a split Hopkinson pressure bar and electron probe microanalyzer and scanning electron microscope. The $(Al_{0.5}CoCrFeNi)_{0.95}Mo_{0.025}C_{0.025}$ HEA has a uniform face-centered cubic plus body-centered cubic solid solution structure and a fine grain-sized microstructure with a size of about 2 microns. The HEA possesses an excellent strain hardening rate and high strain rate sensitivity at a high strain rate. The Johnson–Cook plastic model was used to describe the dynamic flow behavior. Hat-shaped specimens with different nominal strain levels were used to investigate forced shear localization. After dynamic deformation, a thin and short shear band was generated in the designed shear zone and then the specimen quickly fractured along the shear band.

Keywords: high entropy alloy; mechanical properties; high strain rate; shear band; microstructure

1. Introduction

High entropy alloys (HEAs) contain at least five elements in equiatomic or near-equiatomic ratios and have excellent properties [1–4]. They tended to form a simple solid-solution phase when first proposed by Yeh et al. [5]. With the further study of HEAs, multiphase HEAs became more and more common. As a broad category of HEAs, the $Al_xCoCrFeNi$ HEAs have aroused huge interest from researchers since the appearance of HEAs. The crystal structure of the $Al_xCoCrFeNi$ alloys transforms from face-centered cubic (FCC) to body-centered cubic (BCC) with an increase in Al content [6–8]. Meanwhile, the properties of HEAs, such as hardness, electrical conductivity, and thermal conductivity, also change with the transformation of the structure [6,7]. Lin et al. [9] investigated the microstructure, hardness, and corrosion properties of the $Al_{0.5}CoCrFeNi$ alloys aged at different temperatures and found that an FCC + BCC solid solution structure with optimal hardness appeared when the alloys were aged at 350–800 °C. Niu et al. [10] studied the strengthening of nanoprecipitations in an annealed $Al_{0.5}CoCrFeNi$ HEA and found that the nano-sized BCC phase particles reinforced the $Al_{0.5}CoCrFeNi$ HEA. Wang et al. [11] discovered that the temperature of the FCC to BCC phase transformation in the $Al_{0.5}CoCrFeNi$ HEA was 1044 K, and the tensile strength increased after phase transformation. Therefore, previous works showed that the existence of the FCC + BCC solid solution structure is beneficial for improving the mechanical properties of the $Al_{0.5}CoCrFeNi$ alloy. Regarding the effects of the addition of Mo and C elements to HEAs, the addition of Mo could cause solution strengthening because of the large atomic size [12–15]. Additionally, Zhuang et al. [16] found that the addition of

Mo into $Al_{0.5}CoCrFeNi$ HEA could enhance the formation of a (Cr, Mo)-rich σ phase and adjust the mechanical properties of the $Al_{0.5}CoCrFeNiMo_x$ HEAs, including hardness, strength, and ductility. Jian et al. [17] suggested that the addition of C could promote the formation of carbides and induce precipitation strengthening. Jian et al. [17] also found that carbide precipitation could inhibit grain growth during recrystallization. The powder metallurgy method provides a promising way to prepare the $Al_{0.5}CoCrFeNi$ HEA reinforced by Mo and C elements.

Many materials researchers are paying more and more attention to the dynamic mechanical properties of HEAs for industry application. Kumar et al. [18] reached the conclusion that the deformation mechanism of the $Al_{0.1}CrFeCoNi$ HEA at a high strain rate is the same as that of low stacking fault energy materials. Dirras et al. [19] found that the yield strength in the $Ti_{20}Hf_{20}Zr_{20}Ta_{20}Nb_{20}$ HEA was much higher under dynamic loading conditions than under quasi-static conditions and observed a shear band in the dynamic regime. Wang et al. [20] investigated the serration behavior and microstructure of the CoCrFeMnNi HEA prepared by powder metallurgy at strain rates from 1×10^{-4} s^{-1} to 1×10^{-1} s^{-1} and from 1×10^{3} s^{-1} to 3×10^{3} s^{-1}. Additionally, the dynamic mechanical properties of the as-cast NiCrFeCoMn HEA were investigated by Wang et al. [21]. Ma et al. [22] studied the influence of the strain rate on the dynamic mechanical properties of the $AlCrCuFeNi_2$ HEA and found a linear relationship between the dynamic yield strength and strain rate. Shear localization, or shear band, is the main failure mechanism for the materials deformed under high velocity loading. Li et al. [23] studied the shear localization in the CrMnFeCoNi HEA and revealed that the deformation mechanism was rotational dynamic recrystallization. They also found that the $Al_{0.3}CoCrFeNi$ HEA was unable to form a shear band [24], and they attributed the remarkable resistance to shear failure to the excellent strain hardening ability. An et al. [25] found that the addition of Mo and C elements to the $Al_{0.5}CoCrFeNi$ HEA could significantly increase the tensile strength under quasi-static loading. However, the dynamic mechanical properties of $Al_{0.5}CoCrFeNi$ reinforced by Mo and C are not clear yet.

In this paper, we investigated the microstructure and mechanical behavior of the $(Al_{0.5}CoCrFeNi)_{0.95}Mo_{0.025}C_{0.025}$ HEA prepared by powder extrusion and explored the forced shear localization of the $(Al_{0.5}CoCrFeNi)_{0.95}Mo_{0.025}C_{0.025}$ HEA.

2. Materials and Methods

High purity Al, Co, Cr, Fe, Ni, Mo, and C powders of a nominal composition $(Al_{0.5}CoCrFeNi)_{0.95}Mo_{0.025}C_{0.025}$ (at.%) were melted in an induction heated vacuum furnace. Then, the melt was drop through a ceramic tube and atomized by high purity Ar with a pressure of 4 MPa. After cooling down the gas-atomized powder in the atomization chamber, a stainless can with dimensions of φ 60 mm × 150 mm, which was degassed for 12 h at a temperature of 500 °C and sealed in a vacuum, was used to fill the as-prepared HEA powder. The encapsulated powder was then pre-heated for 1 h at a temperature of 1150 °C and immediately hot extruded into bars with an extrusion ratio of 6. After hot extrusion, the bar was cooled in the air. The content of oxygen in the gas-atomized powder was 750 ppm, and the chemical compositions of the $(Al_{0.5}CoCrFeNi)_{0.95}Mo_{0.025}C_{0.025}$ HEA are listed in Table 1.

Table 1. The chemical compositions of the high entropy alloys (HEA).

Elements	Al	Co	Cr	Fe	Ni	Mo	C
(wt.%)	4.54	23.92	23.25	20.90	22.19	4.49	0.71
(at.%)	9.0	21.7	23.9	20.0	20.2	2.5	2.7

For an n-element multicomponent alloy at a random state, the configurational entropy ΔS_{mix} can be calculated according to Boltzmann's hypothesis by the following equation [26]:

$$\Delta S_{mix} = -R \sum_{i=1}^{n} (x_i \ln x_i) \quad (1)$$

where R is the gas constant and has a value of 8.314 JK^{-1} mol^{-1}, n is the number of total elements, and x_i is the concentration of element i.

By substituting the actual compositions of $(Al_{0.5}CoCrFeNi)_{0.95}Mo_{0.025}C_{0.025}$ HEA, the configurational entropy ΔS_{mix} can be calculated as 1.725R, which satisfies the definition of HEA [27].

The produced material was observed using a POLYVAR-MET optical microscope (OM, Leica, Germany) and a JXA-8230 electron probe microanalyzer (EPMA, JEOL, Japan). The etchant for the $(Al_{0.5}CoCrFeNi)_{0.95}Mo_{0.025}C_{0.025}$ HEA was 25 mL hydrochloric acid + 25 mL ethyl alcohol + 5 g $CuSO_4{\cdot}5H_2O$. An X-ray diffraction (XRD) test was also performed on a Rigaku 2550 diffractometer (Rigaku, Japan) using Cu radiation to analyze the structure of the as-received $(Al_{0.5}CoCrFeNi)_{0.95}Mo_{0.025}C_{0.025}$ HEA.

To obtain the mechanical properties of the $(Al_{0.5}CoCrFeNi)_{0.95}Mo_{0.025}C_{0.025}$ HEA, cylinder specimens were used for quasi-static compression tests and dynamic load tests. The cylinder specimens were cut from the as-received HEA bars along the extrusion direction (ED) with dimensions of φ 4 mm × 5.6 mm. The quasi-static compression tests were performed on INSTRON 8802 (Instron, the USA) with strain rates of 1×10^{-1}, 1×10^{-2}, and 1×10^{-3} s^{-1}. The dynamic load tests were performed on a split Hopkinson pressure bar (SHPB, Beijing Xiaotu Technology Co., Ltd, China) with strain rates of 550, 1300, 2200, and 3000 s^{-1}. Hat-shaped specimens cut along the ED were used to induce forced shear localization, as shown in Figure 1. The shadow parts show the designed shear zones of the specimen. Measured sizes of the hat-shaped specimens of designed shear zones are shown in the Table 2. The nominal strain was $\gamma_{nom.} = 2 \times (f_{before} - f_{after})/(b_{before} - a_{before})$. After dynamic deformation, hat-shaped specimens were observed using a Quanta-200 scanning electron microscope (SEM, FEI, Netherlands).

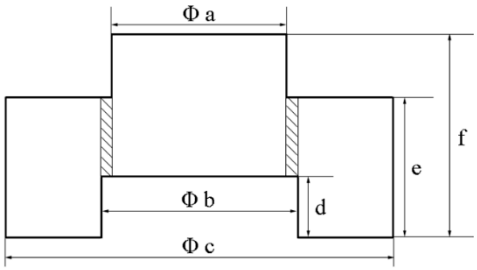

Figure 1. The diagram of the hat-shaped specimen.

Table 2. Measured sizes of the hat-shaped specimens (dimensions in mm).

		a	b	c	d	e	f	$\gamma_{nom.}$
1	before	5.70	6.00	12.80	1.98	4.70	6.88	2.53
	after	5.96	6.00	12.84	1.78	4.64	6.50	
2	before	5.90	6.30	13.14	1.98	5.00	7.00	5.30
	after	6.20	6.58	13.26	1.00	4.98	5.94	
3	before	5.76	6.00	12.86	1.94	4.70	6.88	9.83
	after	5.92	6.00	12.90	0.90	4.64	5.70	

3. Results and Discussion

3.1. Microstructure of the High Entropy Alloy

Figure 2a shows an optical micrograph of the $(Al_{0.5}CoCrFeNi)_{0.95}Mo_{0.025}C_{0.025}$ HEA. The HEA is composed of fine grains with a size of about 2 microns. Figure 2b shows the XRD pattern of the specimen. The phase composition of the $(Al_{0.5}CoCrFeNi)_{0.95}Mo_{0.025}C_{0.025}$ HEA includes the FFC phase and the BCC phase. The chemical compositions of the phases were identified by an electron probe technique, as shown in Figure 3 and Table 3. It was found that the $(Al_{0.5}CoCrFeNi)_{0.95}Mo_{0.025}C_{0.025}$ HEA consists

of a light gray FCC matrix phase (marked as point 1), a black (Al, Ni)-rich BCC phase (marked as point 2), and a gray (Cr, Mo, C)-rich $M_{23}C_6$ carbide phase (marked as point 3). This shows that the C element exists in the $M_{23}C_6$ carbide phase and the Mo element exists in the FCC matrix phase and $M_{23}C_6$ phase, and the MoC phase can also be identified in the Mo-rich $M_{23}C_6$ carbide phase. Figure 3b displays that the distributions of the FCC, BCC, and $M_{23}C_6$ phases in the $(Al_{0.5}CoCrFeNi)_{0.95}Mo_{0.025}C_{0.025}$ HEA are uniform.

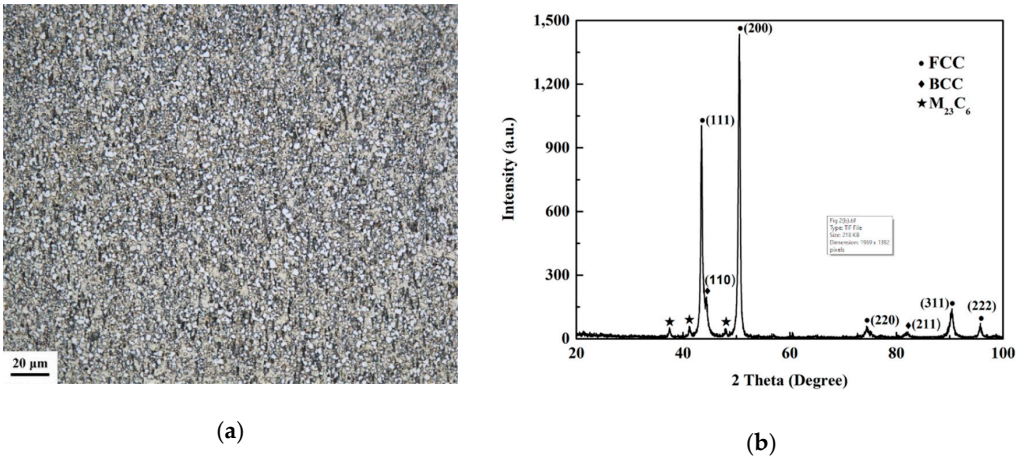

(**a**) (**b**)

Figure 2. Microstructure of the $(Al_{0.5}CoCrFeNi)_{0.95}Mo_{0.025}C_{0.025}$ HEA. (**a**) Optical micrograph; (**b**) XRD pattern.

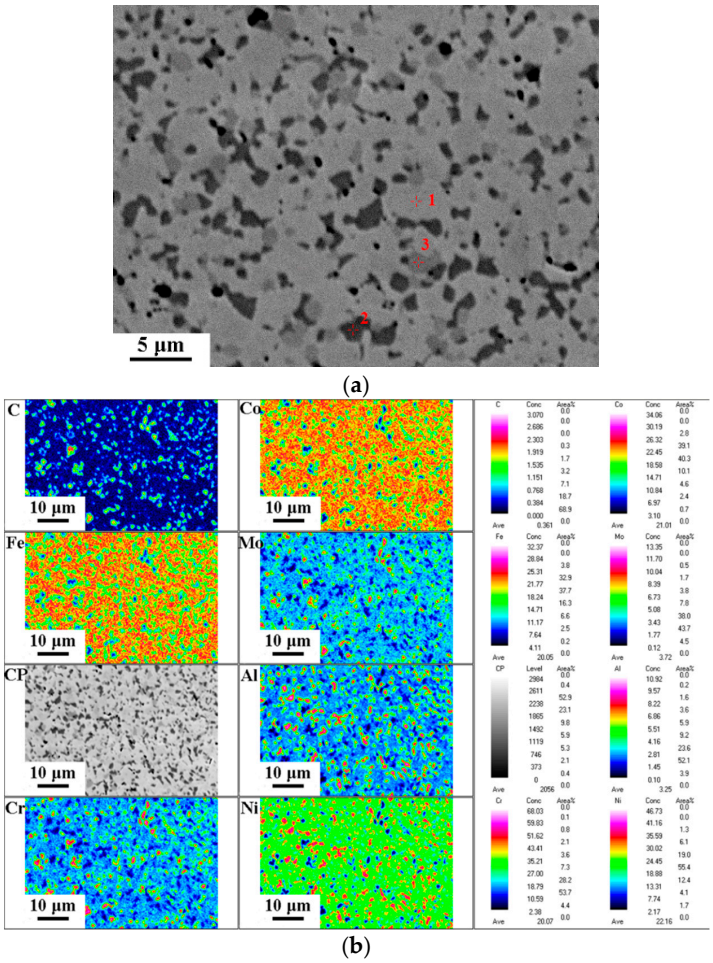

(**a**)

(**b**)

Figure 3. The electron probe microanalyzer (EPMA) maps of the $(Al_{0.5}CoCrFeNi)_{0.95}Mo_{0.025}C_{0.025}$ HEA. (**a**) The phase composition; (**b**) element distribution maps.

Table 3. The average chemical compositions of phases determined by EPMA (in at.%). BCC: body-centered cubic, FCC: face-centered cubic.

Phases	Al	Co	Cr	Fe	Ni	Mo	C
FCC	7.7	24.5	18.3	23.5	20.8	2.2	3.0
BCC	27.3	18.5	6.4	13.0	32.2	0.3	2.3
$M_{23}C_6$	1.1	6.7	55.9	9.4	3.2	5.8	17.9

3.2. Stress–Strain Curves of the High Entropy Alloy

Figure 4a shows the engineering stress–strain curves of the $(Al_{0.5}CoCrFeNi)_{0.95}Mo_{0.025}C_{0.025}$ HEA tested at strain rates of 1×10^{-1}, 1×10^{-2}, and 1×10^{-3} s^{-1}. The cylinder specimen exhibited yield strengths of 702, 703, and 716 MPa at strain rates of 1×10^{-3}, 1×10^{-2}, and 1×10^{-1} s^{-1}, respectively. Therefore, with the increase of strain rates under quasi-static compression tests, the yield strength of the $(Al_{0.5}CoCrFeNi)_{0.95}Mo_{0.025}C_{0.025}$ HEA increased. It also can be observed from Figure 4b that light saw-like curves exist in quasi-static compression strain–stress curves.

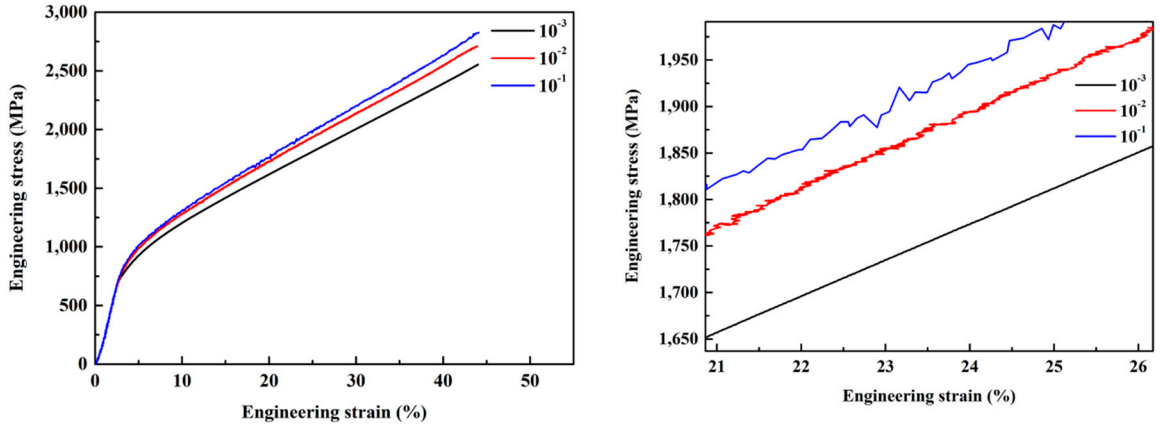

Figure 4. The engineering stress–strain curves of the $(Al_{0.5}CoCrFeNi)_{0.95}Mo_{0.025}C_{0.025}$ HEA tested at the strain rates of 1×10^{-1}, 1×10^{-2}, and 1×10^{-3} s^{-1}; (**b**) the enlarged image of (**a**).

Figure 5 shows the true stress–strain curves of the $(Al_{0.5}CoCrFeNi)_{0.95}Mo_{0.025}C_{0.025}$ HEA deformed at strain rates of 550, 1300, 2200, and 3000 s^{-1}. The yield strengths of the $(Al_{0.5}CoCrFeNi)_{0.95}Mo_{0.025}C_{0.025}$ HEA were 754, 878, 958, and 1057 MPa at strain rates of 550, 1300, 2200 and 3000 s^{-1}, respectively. The saw-like curves are much serious in dynamic compression strain–stress curves. As we observed from the optical micrograph and EPMA maps, the $(Al_{0.5}CoCrFeNi)_{0.95}Mo_{0.025}C_{0.025}$ HEA has small (Al,Ni)-rich BCC phase particles and $M_{23}C_6$ phase particles. The saw-like curves could be attributed to the interaction between the dislocation and (Al,Ni)-rich BCC phase particles plus the $M_{23}C_6$ phase particles.

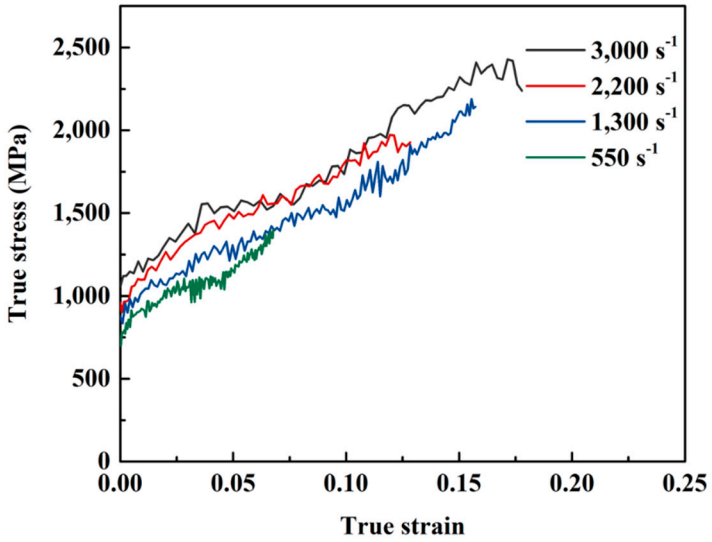

Figure 5. The true stress–strain curves of the $(Al_{0.5}CoCrFeNi)_{0.95}Mo_{0.025}C_{0.025}$ HEA tested at strain rates of 550, 1300, 2200 and 3000 s^{-1}.

The trend of the yield strength of the $(Al_{0.5}CoCrFeNi)_{0.95}Mo_{0.025}C_{0.025}$ HEA at quasi-static and dynamic loading tests is presented in Figure 6. The yield strength increased as a function of the strain rate, and the strain rate sensitivity m can be defined as follows:

$$m = \frac{d(log\sigma)}{d\left(log\dot{\varepsilon}\right)} \tag{2}$$

where σ and $\dot{\varepsilon}$ are the yield strength and strain rate, respectively.

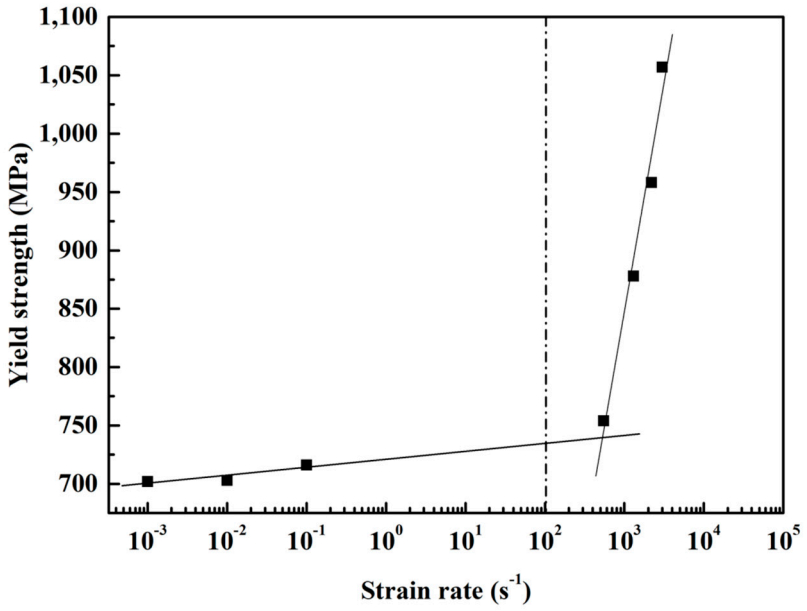

Figure 6. The strain rate sensitivity of the $(Al_{0.5}CoCrFeNi)_{0.95}Mo_{0.025}C_{0.025}$ HEA.

The value of strain rate sensitivity under quasi-static testing conditions was 4.29×10^{-3}, and the value of strain rate sensitivity under dynamic loading conditions was 0.192, which shows a strong strain-rate dependence of the $(Al_{0.5}CoCrFeNi)_{0.95}Mo_{0.025}C_{0.025}$ HEA at high strain rates.

The Johnson–Cook model, which is considered to have a huge strain, high strain rate, and high temperature, was used in this work to describe the plastic deformation of the $(Al_{0.5}CoCrFeNi)_{0.95}Mo_{0.025}C_{0.025}$ HEA. The equivalent flow stress σ can be expressed by the following equation:

$$\sigma = (A + B\varepsilon^n)\left(1 + Cln\dot{\varepsilon}^*\right) \quad (3)$$

where A, B, and C are material constants, and ε and n are the equivalent plastic strain and the strain hardening exponent, respectively. $\dot{\varepsilon}^*$ is the normalized strain rate which can be expressed as $\dot{\varepsilon}^* = \dot{\varepsilon}/\dot{\varepsilon}_0$, where $\dot{\varepsilon}$ is the strain rate and $\dot{\varepsilon}_0$ is a reference strain rate that is equal to 1×10^{-3} s^{-1}. Using the Matlab program (MathWorks, the US, Natick, Version 7.0) to fit the digital matrix of the stress–strain–strain rate, the parameter values and the Johnson–Cook physical equation for the $(Al_{0.5}CoCrFeNi)_{0.95}Mo_{0.025}C_{0.025}$ HEA were obtained. The Johnson–Cook model can describe the plastic deformation of the HEA at high strain rates well, as shown in Figure 7.

$$\sigma = \left(397.1 + 1621\varepsilon^{0.45}\right)\left(1 + 0.05066ln\dot{\varepsilon}^*\right) \quad (4)$$

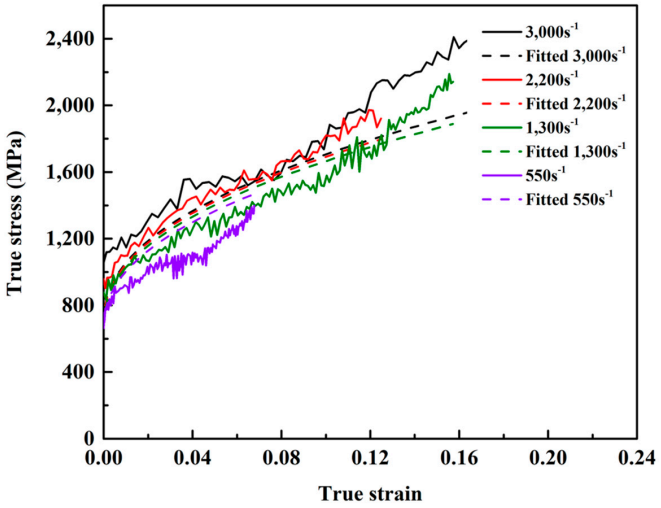

Figure 7. The curves calculated by the Johnson–Cook model compared with experimental curves at the strain rates of 550, 1300, 2200, and 3000 s^{-1}.

The strain hardening rate (dσ/dε) curve for the $(Al_{0.5}CoCrFeNi)_{0.95}Mo_{0.025}C_{0.025}$ HEA at the strain rate of 1×10^{-3} s^{-1} along with the stress–strain curve is shown in Figure 8a. It can be seen that the value of the strain hardening rate was 1621 MPa at a strain level of 0.2, which is much higher than that of most engineering structural alloys, including $Al_xCoCrFeNi$ HEA, as shown in Figure 8b. Therefore, the addition of Mo and C elements can improve the strain hardening rate of $Al_xCoCrFeNi$ HEA.

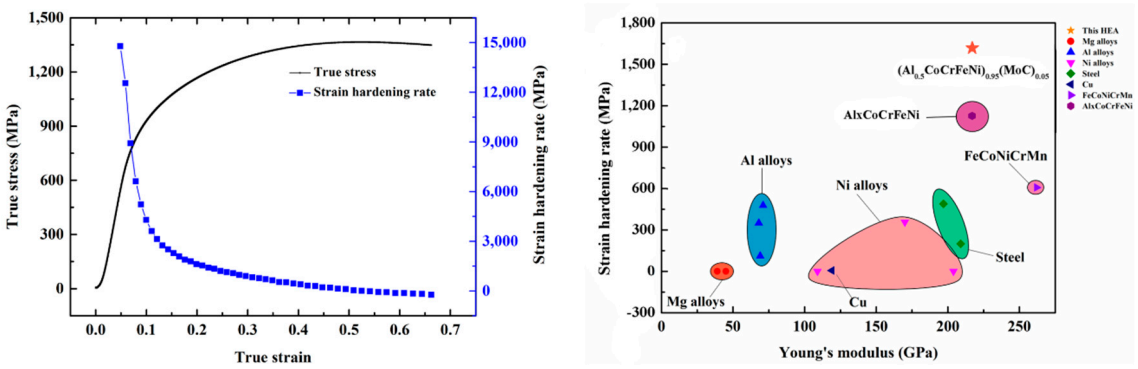

Figure 8. (**a**) The strain hardening rate (dσ/dε) and stress versus strain of the $(Al_{0.5}CoCrFeNi)_{0.95}Mo_{0.025}C_{0.025}$ HEA at a strain rate of 10^{-3} s^{-1}; (**b**) the strain hardening rate of the $(Al_{0.5}CoCrFeNi)_{0.95}Mo_{0.025}C_{0.025}$ HEA compared with other engineering structural alloys.

3.3. Shear Localization of the High Entropy Alloy

Figure 9 shows the hat-shaped specimens with different nominal strain levels used to investigate the forced shear localization of the $(Al_{0.5}CoCrFeNi)_{0.95}Mo_{0.025}C_{0.025}$ HEA. The hat-shaped specimen with a nominal strain of 2.53 was plastically deformed after dynamic deformation, and a small crack was generated at the upper part of the specimen, as shown in Figure 9a. When the designed nominal strain increased to 5.30, the designed shear zones in the hat-shaped specimen consisted of a predominant fracture zone and a small deformation zone, as shown in Figure 9b. Figure 9c is an enlarged view of the red rectangle in Figure 9b, and a short shear band with a width of about 10 microns can be observed. When the designed nominal strain increased to 9.83, the hat-shaped specimen was fractured, as shown in Figure 9d. Some dimples and streamlines were observed along the shear direction, as shown in Figure 9e, which mean that shear bands were generated and then the specimen rapidly fractured along the shear band.

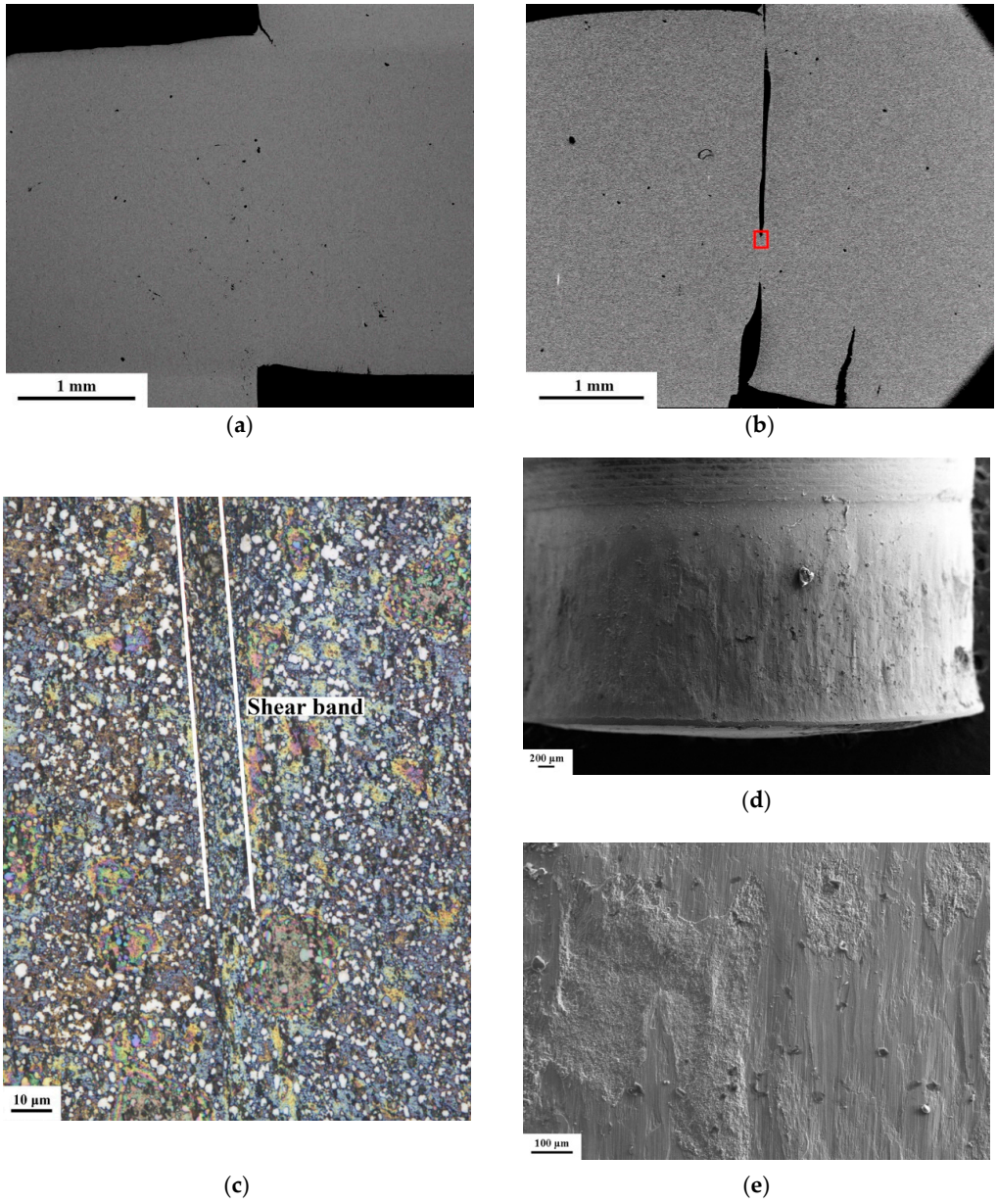

Figure 9. Microstructures of hat-shaped specimens with different nominal strains. (**a**) SEM graph for the specimen with a nominal strain of 2.53; (**b**) SEM graph for the specimen with a nominal strain of 5.30; (**c**) optical micrograph of the shear zone; (**d**) SEM graph for the specimen with a nominal strain of 9.83; (**e**) enlarged image of (**d**).

The formation of the shear band can be attributed to the instability of thermal viscoplastic behavior. The critical condition of the constitutive instability can be expressed as

$$\frac{d\tau}{d\gamma} = \frac{\partial \tau}{\partial \gamma} + \frac{\partial \tau}{\partial \dot{\gamma}} \frac{d\dot{\gamma}}{d\gamma} + \frac{\partial \tau}{\partial T} \frac{dT}{d\gamma} < 0 \tag{5}$$

where τ is the shear stress, γ is the shear strain, and $\dot{\gamma}$ is the shear strain rate.

The strain hardening ($\frac{\partial \tau}{\partial \gamma}$) and strain rate hardening ($\frac{\partial \tau}{\partial \dot{\gamma}}$) values are greater than 0, and the thermal softening ($\frac{\partial \tau}{\partial T}$) value is less than 0. When the value of thermal softening is greater than the values of strain hardening and strain rate hardening, shear localization happens. Li et al. [24] investigated the shear localization of $Al_{0.3}$CoCrFeNi HEA and found the value of strain hardening was greater than the

value of thermal softening, which explains the failure of the $Al_{0.3}CoCrFeNi$ HEA to form a shear band. In our work, with the addition of the Mo and C elements, the $(Al_{0.5}CoCrFeNi)_{0.95}Mo_{0.025}C_{0.025}$ HEA had a much higher strain hardening rate than that of the $Al_{0.3}CoCrFeNi$ HEA. However, the shear band was generated in the $(Al_{0.5}CoCrFeNi)_{0.95}Mo_{0.025}C_{0.025}$ HEA. This was due to the dissolved Mo atoms in the matrix phase, which hinder the heat diffusion, thus decreasing the thermal conductivity. The decreasing of thermal conductivity can increase the value of thermal softening, therefore promoting the generation of shear bands. Because of the high strain hardening rate and low interfacial strength [25], the shear band is very short and easily fractured along the shear direction. However, it shows that the shear band can coordinate deformation in the $(Al_{0.5}CoCrFeNi)_{0.95}Mo_{0.025}C_{0.025}$ HEA under high velocity loading.

4. Conclusions

The $(Al_{0.5}CoCrFeNi)_{0.95}Mo_{0.025}C_{0.025}$ HEA prepared by powder extrusion has a uniform FCC + BCC solid solution structure and consists of the FCC matrix phase, the (Al, Ni)-rich BCC phase, and the (Cr, Mo, C)-rich $M_{23}C_6$ carbide phase. The MoC phase can also be identified in the Mo-rich $M_{23}C_6$ carbide phase. The $(Al_{0.5}CoCrFeNi)_{0.95}Mo_{0.025}C_{0.025}$ HEA shows a strong strain rate sensitivity at high strain rates, and the yield strength of the HEA increases from 754 to 1057 MPa as the strain rate increases from 550 to 3000 s^{-1}. The Johnson–Cook model was used to describe the dynamic flow behavior. The addition of Mo and C elements can improve the strain hardening rate of the $Al_xCoCrFeNi$ HEA. A short shear band of about 10 microns in width was generated in the designed shear zone and then the specimen quickly fractured along the shear band, which indicates that the shear band can coordinate deformation in the $(Al_{0.5}CoCrFeNi)_{0.95}Mo_{0.025}C_{0.025}$ HEA under high velocity loading.

Author Contributions: Conceptualization, B.W. and B.L.; methodology, B.W.; software, C.W.; validation, B.W.; B.L. and X.Z.; formal analysis, B.W. and C.W.; investigation, C.W.; resources, B.W.; data curation, C.W.; writing-original draft preparation, C.W.; writing-review and editing, B.W. and C.W.; supervision, B.W.; project administration, B.W., B.L. and X.Z.; funding acquisition, B.W., B.L. and X.Z.

Funding: This work was funded by the National Natural Science of China (No. 51771231) and by Scientific and Technological Innovation Projects of Hunan Province, China (No. 2017GK2292) by the State Key Laboratory of Powder Metallurgy (No. 621021721).

Acknowledgments: The authors wish to express their most sincere gratitude to M. A. Meyers at the University of California, San Diego and Yong Liu at Central South University for their advice and help. The authors would like to express their heartfelt gratitude to Xiang Zan at the Hefei University of Technology for dynamic testing.

Conflicts of Interest: The authors declare no conflict of interest.

References

1. Huang, S.; Li, W.; Li, X.Q.; Schönecker, S.; Bergqvist, L.; Holmström, E.; Varga, L.K.; Vitos, L. Mechanism of magnetic transition in FeCrCoNi-based high entropy alloys. *Mater. Des.* **2016**, *103*, 71–74. [CrossRef]
2. Zhang, A.J.; Han, J.S.; Su, B.; Li, P.D.; Meng, J.H. Microstructure, mechanical properties and tribological performance of CoCrFeNi high entropy alloy matrix self-lubricating composite. *Mater. Des.* **2017**, *114*, 253–263. [CrossRef]
3. Tang, Q.H.; Huang, Y.; Cheng, H.; Liao, X.Z.; Langdon, T.G.; Dai, P.Q. The effect of grain size on the annealing-induced phase transformation in an $Al_{0.3}CoCrFeNi$ high entropy alloy. *Mater. Des.* **2016**, *105*, 381–385. [CrossRef]
4. Zhang, Y.; Zuo, T.T.; Tang, Z.; Gao, M.C.; Dahmen, K.A.; Liaw, P.K.; Lu, Z.P. Microstructures and properties of high-entropy alloys. *Prog. Mater. Sci.* **2014**, *61*, 1–93. [CrossRef]
5. Yeh, J.W.; Chen, S.K.; Lin, S.J.; Gan, J.Y.; Chin, T.S.; Shun, T.T.; Tsau, C.H.; Chang, S.Y. Nanostructured high-entropy alloys with multiple principal elements: Novel alloy design concepts and outcomes. *Adv. Eng. Mater.* **2004**, *6*, 299–303. [CrossRef]
6. Chou, H.P.; Chang, Y.S.; Chen, S.K.; Yeh, J.W. Microstructure, thermophysical and electrical properties in $Al_xCoCrFeNi$ ($0 \leq x \leq 2$) high-entropy alloys. *Mater. Sci. Eng. B* **2009**, *163*, 184–189. [CrossRef]
7. Wang, W.R.; Wang, W.L.; Wang, S.C.; Tsai, Y.C.; Lai, C.H.; Yeh, J.W. Effects of Al addition on the microstructure and mechanical property of AlxCoCrFeNi high-entropy alloys. *Intermetallics* **2012**, *26*, 44–51. [CrossRef]

8. Yang, T.F.; Xia, S.Q.; Liu, S.; Wang, C.X.; Liu, S.S.; Zhang, Y.; Xue, J.M.; Yan, S.; Wang, Y.G. Effects of AL addition on microstructure and mechanical properties of Al_xCoCrFeNi High-entropy alloy. *Mater. Sci. Eng. A* **2015**, *648*, 15–22. [CrossRef]
9. Lin, C.M.; Tsai, H.L. Evolution of microstructure, hardness, and corrosion properties of high-entropy Al0.5CoCrFeNi alloy. *Intermetallics* **2011**, *19*, 288–294. [CrossRef]
10. Niu, S.Z.; Kou, H.C.; Guo, T.; Zhang, Y.; Wang, J.; Li, J.S. Strengthening of nanoprecipitations in an annealed $Al_{0.5}$CoCrFeNi high entropy alloy. *Mater. Sci. Eng. A* **2016**, *671*, 82–86. [CrossRef]
11. Wang, J.; Niu, S.Z.; Guo, T.; Kou, H.C.; Li, J.S. The FCC to BCC phase transformation kinetics in an $Al_{0.5}$CoCrFeNi high entropy alloy. *J. Alloys Compd.* **2017**, *710*, 144–150. [CrossRef]
12. Liu, W.H.; Lu, Z.P.; He, J.Y.; Luan, J.H.; Wang, Z.J.; Liu, B.; Liu, Y.; Chen, M.W.; Liu, C.T. Ductile CoCrFeNiMo$_x$ high entropy alloys strengthened by hard intermetallic phases. *Acta Mater.* **2016**, *116*, 332–342. [CrossRef]
13. Shun, T.T.; Chang, L.Y.; Shiu, M.H. Microstructure and mechanical properties of multiprincipal component CoCrFeNiMo$_x$ alloys. *Mater. Charact.* **2012**, *70*, 63–67. [CrossRef]
14. Li, W.P.; Wang, X.G.; Liu, B.; Fang, Q.H.; Jiang, C. Fracture mechanisms of a Mo alloyed CoCrFeNi high entropy alloy: In-situ SEM investigation. *Mater. Sci. Eng. A* **2018**, *723*, 79–88. [CrossRef]
15. Cai, B.; Liu, B.; Kabra, S.; Wang, Y.Q.; Yan, K.; Lee, P.D.; Liu, Y. Deformation mechanisms of Mo alloyed FeCoCrNi high entropy alloy: In situ neutron diffraction. *Acta Mater.* **2017**, *127*, 471–480. [CrossRef]
16. Zhuang, Y.X.; Zhang, X.L.; Gu, X.Y. Effect of molybdenum on phases, microstructure and mechanical properties of $Al_{0.5}$CoCrFeMoxNi high entropy alloys. *J. Alloys Compd.* **2018**, *743*, 514–522. [CrossRef]
17. Peng, J.; Li, Z.Y.; Fu, L.M.; Ji, X.B.; Pang, Z.R.; Shan, A.D. Carbide precipitation strengthening in fine-grained carbon-doped FeCoCrNiMn high entropy alloy. *J. Alloys Compd.* **2019**, *803*, 491–498. [CrossRef]
18. Kumar, N.; Ying, Q.; Nie, X.; Mishra, R.S.; Tang, Z.; Liaw, P.K.; Brennan, R.E.; Doherty, K.J.; Cho, K.C. High strain-rate compressive deformation behavior of the $Al_{0.1}$CrFeCoNi high entropy alloy. *Mater. Des.* **2015**, *86*, 598–602. [CrossRef]
19. Dirras, G.; Couque, H.; Lilensten, L.; Heczel, A.; Tingaud, D.; Couzinie, J.P.; Perriere, L.; Gubicza, J.; Guillot, I. Mechanical behavior and microstructure of $Ti_{20}Hf_{20}Zr_{20}Ta_{20}Nb_{20}$ high-entropy alloy loaded under quasi-static and dynamic compression conditions. *Mater. Charact.* **2016**, *111*, 106–113. [CrossRef]
20. Wang, B.F.; Huang, X.X.; Fu, A.; Liu, Y.; Liu, B. Serration behavior and microstructure of high entropy alloy CoCrFeMnNi prepared by powder metallurgy. *Mater. Sci. Eng. A* **2018**, *726*, 37–44. [CrossRef]
21. Wang, B.F.; Yao, X.R.; Wang, C.; Zhang, X.Y.; Huang, X.X. Mechanical Properties and Microstructure of a NiCrFeCoMn High-Entropy Alloy Deformed at High Strain Rates. *Entropy* **2018**, *20*, 892. [CrossRef]
22. Ma, S.G.; Jiao, Z.M.; Qiao, J.W.; Yang, H.J.; Zhang, Y.; Wang, Z.H. Strain rate effects on the dynamic mechanical properties of the AlCrCuFeNi$_2$ high-entropy alloy. *Mater. Sci. Eng. A* **2016**, *649*, 35–38. [CrossRef]
23. Li, Z.Z.; Zhao, S.T.; Alotaibi, S.M.; Liu, Y.; Wang, B.F.; Meyers, M.A. Adiabatic shear localization in the CrMnFeCoNi high-entropy alloy. *Acta Mater.* **2018**, *151*, 424–431. [CrossRef]
24. Li, Z.; Zhao, S.; Diao, H.; Liaw, P.K.; Meyers, M.A. High-velocity deformation of Al0.3CoCrFeNi high-entropy alloy: Remarkable resistance to shear failure. *Sci. Rep.* **2017**, *7*, 42742. [CrossRef]
25. An, Q.; Wang, J.W.; Liu, Y.; Liu, B.; Guo, W.M.; Fang, Q.H.; Nie, Y. Effects of C and Mo on microstructures and mechanical properties of dual-phase high entropy alloys. *Intermetallics* **2019**, *110*, 106471. [CrossRef]
26. Zhou, Y.; Zhou, D.; Jin, X.; Zhang, L.; Du, X.Y.; Li, B.S. Design of non-equiatomic medium-entropy alloys. *Sci. Rep.* **2018**, *8*, 1236. [CrossRef]
27. Yeh, J.W. Alloy design strategies and future trends in high-entropy alloys. *JOM* **2013**, *65*, 1759–1771. [CrossRef]